

SRIF: Semantic Shape Registration Empowered by Diffusion-based Image Morphing and Flow Estimation

MINGZE SUN*, Tsinghua Shenzhen International Graduate School, China

CHEN GUO*, Tsinghua Shenzhen International Graduate School, Peng Cheng Lab, China

PUHUA JIANG*, Tsinghua Shenzhen International Graduate School, Peng Cheng Lab, China

SHIWEI MAO, Tsinghua Shenzhen International Graduate School, China

YURUN CHEN, Tsinghua Shenzhen International Graduate School, China

RUQI HUANG†, Tsinghua Shenzhen International Graduate School, China



Fig. 1. Given two teapots (blue meshes), **SRIF** first generates plausible intermediate point clouds (middle of top row) bridging them based on multi-view image morphing [Zhang et al. 2023] and dynamic 3D Gaussian splatting reconstruction [Huang et al. 2024], and then estimates an invertible normalizing flow that *continuously* deforms the source to the target with the above auxiliary point clouds, resulting in both a semantically meaningful morphing process and high-quality dense correspondences indicated by the accurate texture transfer (bottom row).

In this paper, we propose **SRIF**, a novel **S**emantic shape **R**egistration framework based on diffusion-based **I**mage morphing and **F**low estimation. More concretely, given a pair of extrinsically aligned shapes, we first render them from multi-views, and then utilize an image interpolation framework based on diffusion models to generate sequences of intermediate images between them. The images are later fed into a dynamic 3D Gaussian splatting framework, with which we reconstruct and post-process for intermediate *point clouds* respecting the image morphing processing. In the end, tailored for the above, we propose a novel registration module to estimate continuous normalizing flow, which deforms source shape consistently towards the target, with intermediate point clouds as weak guidance. Our key insight is to leverage large vision models (LVMs) to *associate* shapes and therefore obtain much richer semantic information on the relationship between shapes than the ad-hoc feature extraction and alignment. As consequence, **SRIF** achieves high-quality dense correspondences on challenging shape pairs, but also delivers smooth, semantically meaningful interpolation in between. Empirical evidences justify the effectiveness and superiority of our method as well as specific design choices. The code is released at <https://github.com/rquang88/SRIF>.

CCS Concepts: • **Computing methodologies** → **Shape analysis**.

1 INTRODUCTION

Estimating dense correspondences between 3D shapes serves as a cornerstone in many applications of computer graphics, including

3D reconstruction [Yu et al. 2018], animation [Sumner and Popović 2004] and statistical shape analysis [Anguelov et al. 2005], to name a few. Regarding shapes undergoing rigid or isometric deformations, the prior shape registration/matching techniques [Amberg et al. 2007; Bronstein et al. 2006; Ovsjanikov et al. 2012; PJ and ND 1992] have laid down solid foundations on both theoretical and practical fronts. In this paper, we consider the problem of estimating semantically meaningful dense correspondences between shapes undergoing more general and complicated deformations.

In the absence of a compact deformation prior, the purely geometric methods typically take a coarse-to-fine approach. Namely, one leverages geometric features to locate a small set of landmarks on both shapes, estimates sparse landmark correspondences, and finally propagates dense correspondences via minimizing distortions such as conformal [Kim et al. 2011], elastic energy [Edelstein et al. 2020]. It is worth noting, though, that the sparse correspondences derived from geometry are not necessarily relevant to semantics. As shown in qualitative results in Sec. 4, the resulting maps can suffer from such discrepancy, especially in the presence of significant heterogeneity.

To this end, another line of works concentrate on producing high-quality semantic correspondences at the cost of dependency on

* Equal contribution, † Corresponding to Ruqi Huang (ruqi-huang@sz.tsinghua.edu.cn).

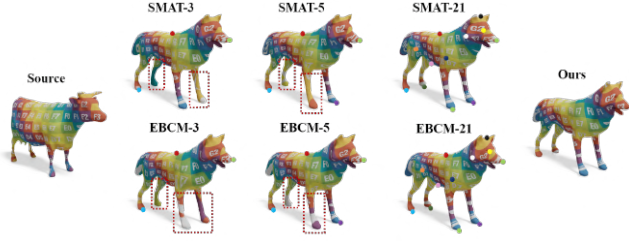


Fig. 2. Maps obtained by state-of-the-art compatible remeshing techniques [Schmidt et al. 2023; Yang et al. 2020] based on varying number of landmark correspondences. The absence of landmarks at local region can lead to erroneous matching (see the red boxes). On the other hand, our method delivers high-quality maps with *no* landmark annotation.

user-defined landmarks [Aigerman et al. 2015; Ezuz et al. 2019; Mandad et al. 2017; Schmidt et al. 2023; Yang et al. 2020]. Treating landmarks as anchor points, they cast the problem as correspondence interpolation, which can be conducted by optimizing certain geometric distortions. However, the dependency on manual annotations limits the practical utility of these works. Apart from hindering automation, insufficient annotation strength can lead to sub-optimal results as shown in Fig. 2.

More recently, the emergence of learning-based techniques has enabled data-driven semantic information extraction. In essence, one can learn canonical structural information from a collection of 3D shapes, which can help to match challenging non-rigid shapes [Eisenberger et al. 2021; Sun et al. 2021], or heterogeneous man-made objects [Deng et al. 2021; Zheng et al. 2021]. Unfortunately, limited by the amount of available 3D data, the above approaches are typically *category-specific*, weakening their practical utility.

On the other hand, boosted by large-scale natural image datasets such as LAION [Schuhmann et al. 2022], large vision (or vision-language) models (LVMs) [OpenAI 2023; Oquab et al. 2023; Radford et al. 2021; Rombach et al. 2022] has attracted considerable attention from the community of 3D shape analysis [Abdelreheem et al. 2023a,b; Morreale et al. 2024; Wimmer et al. 2024]. The shared protocol is to project 3D shapes into multi-view 2D images. The latter can then be fed into LVMs for semantic encoding, which is finally aggregated back to 3D shapes for the respective task. While the above approach has been proven simple yet effective, we observe that 1) the distilled semantic information is in general coarse (e.g., segmented regions or sparse landmarks); 2) there exists a clear gap between multi-view images rendered from textureless 3D shapes and natural images on which LVMs are trained, the feature extracted from LVMs can be noisy; 3) many approaches leverage the semantics in a simple feed-forward manner and therefore require complicated filtering schemes to ensure reliability [Morreale et al. 2024].

We believe the above issues originate from the fact that LVMs are used to extract features from shapes in a *static, independent* manner, which can be problematic when the shapes are distinct from each other. In light of this, we propose **SRIF**, a framework for **S**emantic shape **R**egistration, which is built with diffusion-based **I**mage morphing and **F**low estimation. The key insight of **SRIF** is to take a *dynamic* viewpoint of leveraging LVMs to associate 3D shapes. More specifically, given a pair of extrinsically aligned

shapes, we first render them from multi-views, then we utilize a diffusion-based image interpolation framework [Zhang et al. 2023] to generate sequences of intermediate images between corresponding views. Then we reconstruct the intermediate point clouds from the interpolated images via a dynamic 3D Gaussian splatting reconstruction framework [Huang et al. 2024] and our surface point extractor tailored for the reconstructed Gaussians. Note that, with the above procedures, we have not achieved any *explicit* connection between the input shapes. Nevertheless, the intermediate point clouds carry rich information on how the shapes are associated from the viewpoint of LVMs. Last but not least, inspired by the dynamic nature of the extracted semantics, we formulate the shape registration problem as estimating a *flow* that deforms source shape towards the target, with the intermediate point clouds as guidance. In particular, we adopt the framework of PointFlow [Yang et al. 2019] into our pipeline and learn a Multi Layer Perception (MLP) to represent as well as optimize for the flow.

We extensively evaluate **SRIF** on a wide range of shape pairs from SHREC’07 dataset [Giorgi et al. 2007] and EBCM [Yang et al. 2020]. Empirical evidence demonstrates that **SRIF** outperforms the competing baselines in all test sets. As shown in Fig. 1 and Sec. 4, **SRIF** not only delivers high-quality dense correspondences between shapes but also generates a continuous, semantically meaningful morphing process, which can potentially contribute to 3D data accumulation.

2 RELATED WORKS

2.1 Dense Shape Correspondence Estimation

Since estimating 3D shape correspondence is an extensively studied area, we refer readers to [Tam et al. 2013] for a comprehensive survey and focus on the most relevant methods, which are autonomous methods for general shape matching or registration.

Axiomatic methods typically follow a coarse-to-fine manner, which depends on sparse landmark correspondences to achieve dense ones. The typical approaches [Edelstein et al. 2020; Kim et al. 2011] first extract and match landmarks using geometric features, and then independently or jointly optimize for dense correspondences based on certain distortion quantity, such as conformality, smoothness. On the other hand, there exists a line of works leveraging fuzzy correspondences [Ovsjanikov et al. 2012] to alleviate under-constrained space of dense maps. For instance, MapTree [Ren et al. 2020] exploits the space of functional maps, SmoothShells [Eisenberger et al. 2020] jointly estimate registration transform in both spatial and functional space. As mentioned before, correspondences derived from geometry do not always align with semantics, especially in the presence of heterogeneity. Our method enjoys the semantic information from LVMs for accurate correspondence estimation.

Learning-based methods take advantage of prior knowledge extracted by networks. According to the sources of prior knowledge, we further classify them as follows:

1) *Large Vision Models (LVMs)*: SATR [Abdelreheem et al. 2023b] renders 3D shapes into multi-view images, gathers coarse semantic labels as part segmentation from each view, and finally back-projects to 3D shapes. Similarly to the axiomatic methods, such cues can be further post-processed with off-the-shelf methods like

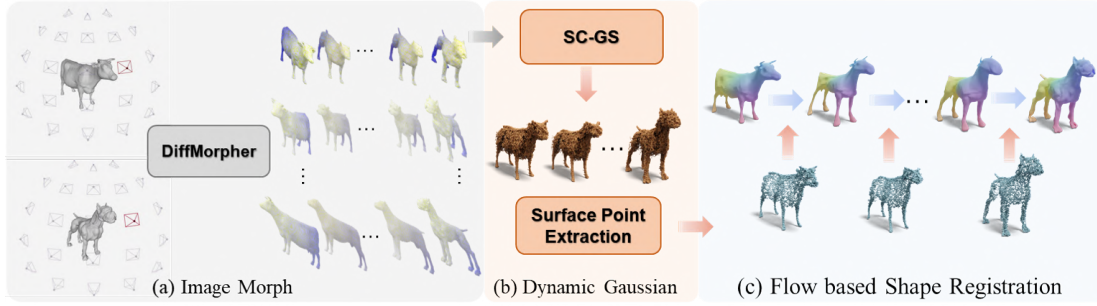


Fig. 3. Our pipeline mainly contains three blocks. (a) Given two extrinsically aligned shapes, we first render them from multi-views, and then use DiffMorpher [Zhang et al. 2023] to generate image interpolation with respect to each views. (b) We then use SC-GS 3D Gaussian Splatting [Yang et al. 2023] to reconstruct, from which we obtain a set of dense and noisy point clouds (in gold). They are fed into our surface point extraction module to obtain clean intermediate point clouds (in blue). (c) Finally, we estimate a continuous normalizing flow, represented by an MLP, that deforms the source to the target under the guidance of the extracted intermediate point clouds (in blue).

functional maps [Ovsjanikov et al. 2012] to achieve dense correspondences [Abdelreheem et al. 2023a]. Since the linguistic signal is not suitable for point-level description, the above approaches suffer from coarse external semantics. It is then highly non-trivial to perform fine-grained shape analysis tasks, including registration. NSSM [Morreale et al. 2024] leverages features from Dinov2 [Oquab et al. 2023] to identify sparse landmark correspondences. Being a two-stage method, NSSM can be fragile regarding the mismatched landmarks. On the other hand, as shown in Fig. 4, **SRIF** is robust with poor semantic information from LVMs.

2) *Category-specific Training* is prevailing in learning-based 3D shape analysis. We identify the most relevant approach along this line as NeuroMorph [Eisenberger et al. 2021], which jointly learns to interpolate and perform registration between shapes. However, NeuroMorph requires pre-training on a small set of 3D shapes, which belongs to the same category as the test ones. Moreover, the interpolation produced by NeuroMorph is dominated by geometric cues, rather than semantics. NeuroMorph is related to our method in the sense that it delivers interpolation as a by-product as well. However, our method generates plausible interpolations *before* estimating correspondences, while NeuroMorph jointly optimizes for both. As suggested by the experimental results, our scheme makes full use of LVMs and surpasses NeuroMorph by a large margin.

2.2 Diffusion Model

Diffusion models [Ho et al. 2020; Rombach et al. 2022] have gained significant popularity recently, thanks to their impressive capacity of learning data distribution from large-scale image datasets. Some recent works [Blattmann et al. 2023; Rombach et al. 2022; Zhao et al. 2023] have attempted to control the generated results and improve the quality of generation. On the other hand, the application of diffusion models in image interpolation receives relatively less attention. During the interpolation process using 2D diffusion models, there is a greater focus on the style of the images rather than on deformation. Want et al. [Wang and Golland 2023] attempt to interpolate in the latent space of diffusion, but the resulting method

suffers from poor generalization capability. On the other hand, DiffMorpher [Zhang et al. 2023] has achieved smooth interpolation based on StableDiffusion. We therefore exploit it in our pipeline as a tool for image morphing, which returns plausible intermediate images encoding the deformations between the source and the target shape.

2.3 3D Gaussian Splatting

As a scene representation, 3D Gaussian Splatting (3D-GS) [Kerbl et al. 2023] represents a 3D scene as a mixture of Gaussian distribution. 3D-GS has dramatically advanced novel view synthesis (NVS) in terms of accuracy and efficiency. Numerous follow-ups have been proposed on 3D-GS, ranging across dynamic NVS [Huang et al. 2024; Yang et al. 2023], SLAM [Keetha et al. 2023], and geometry recovery [Guédon and Lepetit 2023], to name a few.

In particular, our method directly leverages SC-GS [Huang et al. 2024] to reconstruct intermediate geometry from the morphed images. Our point cloud extraction (Sec. 3.2) is similar to mesh extraction from 3D-GS [Guédon and Lepetit 2023], which remains a challenging open problem.

3 METHODOLOGY

SRIF takes as input a pair of meshes (S, T) , which are extrinsically aligned, *i.e.*, roughly in the same up-down and front-back orientation. The desired output is a registered source shape \hat{S} that admits the same triangulation as S and approximates T in geometry. We demonstrate our whole pipeline in Fig. 3, which consists of Image Rendering and Morphing (Sec. 3.1), Intermediate Point Clouds Reconstruction (Sec. 3.2), and Flow Estimation (Sec. 3.3).

3.1 Image Rendering and Morphing

The key sub-goal of our method is to infer an intermediate morphing process between input shapes. Our first step is to employ a diffusion-based image morphing technique, DiffMorpher [Zhang et al. 2023] on multi-view image sets, rendered to both S and T .

Specifically, we pre-process the input shapes such that they are centered around the origin and scaled to be inside a unit sphere. For \mathcal{S} (resp. \mathcal{T}), we render K views, where the viewpoints are sampled uniformly around the shape in the sphere space with a radius of 3.5 length units. We use the renderer from Open3D library [Zhou et al. 2018]. We observe that properly endowing texture to shapes plays a critical role in the follow-up image morphing step. That is because diffusion models [Rombach et al. 2022] are generally trained on realistic images, which are distinctive from straightforward renderings of textureless shapes. To this end, we explore various coloring schemes for rendering shapes and settle down at the following, which integrates spatial coordinate information (see more details in the Supp. Mat.). Given a shape, we denote by z_{\max}, z_{\min} respectively the maximal and minimal value of the z -coordinates of its points, and formulate function $[C_R, C_G, C_B] = [\lfloor \frac{d}{256} \rfloor, \lfloor \frac{d}{256} \rfloor, d - 256 \times \lfloor \frac{d}{256} \rfloor]$ to assign color to each point (x, y, z) , where $d = \lfloor \frac{z - z_{\min}}{z_{\max} - z_{\min}} \times 65535 \rfloor$ and C_R, C_G, C_B are respective the intensity of the RGB channels. The rendered images can be represented as a set of image pairs: $C_r = \{(I_i^{\mathcal{S}}, I_i^{\mathcal{T}}) | i = 1, 2, \dots, K\}$. Subsequently, C_r is processed through an image morphing algorithm DiffMorpher [Zhang et al. 2023], which leverages diffusion models to generate K sequences of intermediate images. This technique allows for a more nuanced and continuous transformation between corresponding views within each image pair in C_r . For each pair, DiffMorpher generates T intermediate images, transitioning from $I_i^{\mathcal{S}}$ to $I_i^{\mathcal{T}}$. Consequently, this process yields $C = \{I_i^j | i = 1, 2, \dots, K; j = 1, 2, \dots, T\}$, a comprehensive image set that captures a wide array of views and detailed morphing stages.

3.2 Intermediate Point Clouds Reconstruction and Post-processing

Note that C contains images sampled from different views as well as different morphing stages. One straightforward way is to reconstruct the intermediate shapes using multi-view reconstruction with images at the same morphing stage. However, since the image morphing is performed independently regarding views, one can hardly guarantee multi-view consistency.

Therefore, we instead formulate the reconstruction as a dynamic one. Moreover, for the sake of efficiency and accuracy, we choose the recent art, SC-GS framework [Huang et al. 2024], for reconstruction. Specifically, we use the vertices of the source mesh to initialize the spatial position of each Gaussian (*i.e.*, mean). From these points, SC-GS creates a set of 3D Gaussians $G(x, r, s, \sigma)$ defined by a center position x , opacity σ , and 3D covariance matrix Σ obtained from quaternion r and scaling s . For a morphing stage $t \in \{1, 2, \dots, T\}$, SC-GS takes the positions x as input and predict the $(\delta x, \delta r, \delta s)$. Subsequently, the deformed 3D Gaussians $G(x + \delta x, r + \delta r, s + \delta s, \sigma)$ is optimized by the differential Gaussian rasterization pipeline. Once optimization is done, given a time step t , we extract the set of positions as the raw intermediate point clouds V_t^G .

Post-processing on V_t^G : First, we deal with outlier points within V_t^G , which comes from the floating Gaussians in the reconstruction. We compute the Euclidean distance between each point and its nearest neighbor in V_t^G , and filter out the ones with distances

larger than a fixed threshold. On the other hand, the adaptive density control module of SC-GS generates additional 3D Gaussians inside the surface of the intermediate shapes. The inner points can be misleading for the registration procedure in Sec. 3.3. To accurately delineate these points, we propose a surface point extraction module. To be precise, given V_t^G , we project depth maps from each facet of a standardized hexahedron. These depth maps are subsequently re-projected as partial viewpoint clouds. After aggregating all these point clouds, we finally obtain the surface point cloud V_t for the registration process. We refer readers to the Supp. Mat. for more detailed descriptions. After the above procedure, there still exists a large amount of points, which can be redundant in the follow-up registration. We thus perform Furthest Point Sampling (FPS) on each V_t such that its number of points is same as that of \mathcal{S} .

3.3 3D Shape Registration via Flow Estimation

Going through the above two main components, we obtain a sequence of intermediate point clouds denoted as $\mathcal{V} = \{V_t | t = 1, \dots, T\}$, each corresponds to a one-time step in image morphing. Without loss of generality, we denote by V_0 the vertices of \mathcal{S} , and V_{T+1} that of \mathcal{T} .

Though it seems natural to iteratively perform shape registration [Amberg et al. 2007] between consecutive point clouds in \mathcal{V} , we observe that this naive approach can lead to sub-optimal results. As shown in the top row of Fig. 4, due to the significant deformation between the cow and the giraffe, the intermediate point clouds are of low quality. Deforming the cow towards such can lead to distortion accumulation (see the middle row of Fig. 4).

In light of this, we propose a more global consistent registration scheme. Namely, we cast the registration problem as estimating a flow that deforms \mathcal{S} towards \mathcal{T} , while approximating the intermediate point clouds at the regarding time steps. As shown in the bottom row of Fig. 4, we achieve high-quality semantic correspondences in this challenging case, while being robust regarding imperfect intermediate guidance.

In particular, we let $y(t)$ be a continuously deforming point cloud with respect to temporal parameter t , such that $y(t_0) = V_0$, our target is then to learn a continuous-time dynamic $\frac{\partial y(t)}{\partial t} = f(y(t), t)$, or, a flow, that indicates how $y(t)$ evolves over time.

In order to estimate the flow, we adopt the framework of PointFlow [Yang et al. 2019]. The key motivations are: 1) to achieve an invertible normalizing flow; 2) to exploit the powerful MLP-based flow representation. In [Yang et al. 2019], f is represented by a neural network with an unrestricted architectural design. A Continuous Normalizing Flow (CNF) models an entity x with an initial prior distribution at the starting time as $x = y(t_0) + \int_{t_0}^{t_1} f(y(t), t) dt$, $y(t_0) \sim P(y)$. The value at $y(t_0)$ can be obtained using the inverse of the flow, expressed as

$$y(t_0) = x + \int_{t_1}^{t_0} f(y(t), t) dt. \quad (1)$$

In our context, we do not assume prior distributions for x and y but rather treat it as a registration problem. Here we set x as the source point cloud \mathcal{S} , and $y(t_0)$ as a prediction of the target point

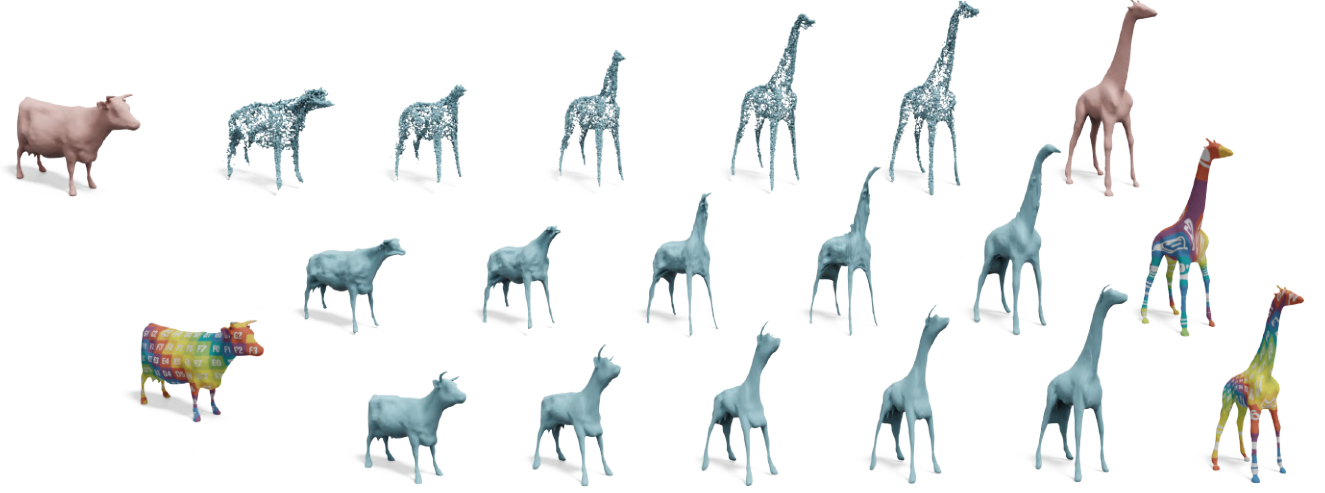


Fig. 4. We select a challenging pair for registration result visualization. The first row shows the point clouds we obtain for guidance, which contain significant noise due to the large deformations undergoing between the shapes. The second row demonstrates the results of using a naive iterative registration approach, which exhibits poor robustness to the noise in the point clouds. The third row displays our results using the continuous normalizing flow, achieving high-quality registration and reasonable intermediate interpolation results.

cloud \mathcal{T} . We define $f(y(t), t)$ as a multi-layer perceptron (MLP). Ultimately, we can obtain the predicted value of the target by solving the ODE (Ordinary Differential Equation) from Eqn. 1.

For fitting the flow, we utilize the following energy function.

$$E_{\text{cd_final}} = CD(y(t_0), V_{T+1}), \quad (2)$$

where CD refers to Chamfer distance, which is widely used to measure the extrinsic distance between two point clouds. To reduce the complexity of optimizing the aforementioned MLP, we sample k discrete time points on the continuous flow as $y(t_k)$. To provide additional guidance throughout the process, we assign functions at specific time points based on the point cloud $\mathcal{V} = \{V_t \mid t = 1, \dots, T\}$ obtained from the previous section. The specific cost function $E_{\text{cd_inter}}$ is.

$$E_{\text{cd_inter}} = \frac{1}{T} \sum_{i \in [T]} CD(y(t_i), V_i). \quad (3)$$

In addition, to ensure the shape does not undergo excessive distortion during the registration process, we include an ARAP (As-Rigid-As-Possible) loss followed by [Guo et al. 2021] as a regularization term. The total cost function E_{total} combines the above terms with the weighting factors $\lambda_{\text{cd_inter}}$, $\lambda_{\text{cd_final}}$, and λ_{arap} to balance them:

$$E_{\text{total}} = \lambda_{\text{cd_inter}} E_{\text{cd_inter}} + \lambda_{\text{cd_final}} E_{\text{cd_final}} + \lambda_{\text{arap}} E_{\text{arap}}. \quad (4)$$

To achieve more accurate registration results, we perform non-rigid shape registration [Amberg et al. 2007] between the output of the flow network and \mathcal{T} .

4 EXPERIMENTAL RESULTS

4.1 Implementation Details

For the input source and target shape, we use Open3D to sample uniformly 16 viewpoints. In particular, empirically we render the background of all rendered images to black for the best overall performance. Note that we demonstrate a white background in Fig. 3, which is for better visualization. We use DiffMorpher [Zhang et al. 2023] to interpolate 10 frames between each pair of images rendered from the same viewpoint. Regarding SC-GS [Huang et al. 2024], we use vertices extracted from the source mesh as the initialization of the mean of Gaussians. The first 3000 iterations of the training step are used for initializing each single Gaussian. Then we train a model to predict the deformation between them, simultaneously optimizing the position, opacity, and covariance matrix for a total of 20000 iterations. We set the percent dense parameter to 0.01 to generate relatively sparse point clouds. In general, we believe in target shape more than the intermediate point clouds. During flow estimation, we set the weight $\lambda_{\text{cd_inter}}$ to 1, that of $\lambda_{\text{cd_final}}$ to 10, and λ_{arap} to 2 for all categories. We train 4000 iterations per pair and the learning rate is set to $1e-3$. We set $t_0 = 0$, $t_1 = 0.5$ and using the 2nd, 4th, 6th and 8th of the $T = 10$ reconstructed point clouds in Eqn. 3.

4.2 Evaluation Setup

Baselines: In this section, we compare our method with an array of methods of estimating dense correspondences, which 1) require no external landmarks as input and 2) pose no constraint (e.g., near-isometry) on the deformations between input shapes: BIM [Kim et al. 2011], SmoothShells [Eisenberger et al. 2020], NeuroMorph [Eisenberger et al. 2021], MapTree [Ren et al. 2020], and ENIGMA [Edelstein et al. 2020]

Table 1. Average geodesic errors on each of the test categories in SHREC07 [Giorgi et al. 2007] and EBCM [Yang et al. 2020].

	Airplane	Ant	Bird	Chair	Fish	Fourleg	Glasses	Human	Plier	EBCM
MapTree	0.5634	0.2635	0.4117	0.4742	0.2949	0.3507	0.6878	0.2633	0.2805	0.4231
BIM	0.2589	0.3050	0.4123	0.4800	0.2699	0.2449	0.6160	0.1810	0.5197	0.2968
SmoothShell	0.2749	0.2694	0.3009	0.2627	0.1032	0.1234	0.3100	0.1572	0.3900	0.4476
NeuroMorph	0.1510	0.1895	0.1672	0.1853	0.1366	0.1697	0.2652	0.2141	0.2830	0.1844
ENIGMA	0.3568	0.3675	0.3278	0.4482	0.1733	0.2466	0.6187	0.2925	0.4379	0.3032
Ours	0.0356	0.1133	0.0965	0.0295	0.0804	0.0824	0.0614	0.1467	0.1476	0.0886

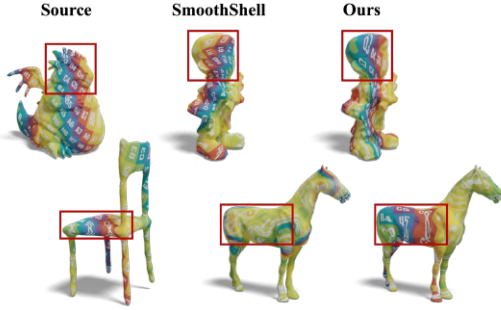


Fig. 5. We match shapes from distinctive categories. Top: Dragon vs. Solider; Bottom: Chair vs. Horse.

Benchmarks: We comprehensively compare our method and the baselines in an array of test sets. (1) We consider 9 categories from SHREC07 dataset [Giorgi et al. 2007] – human, fourleg, airplane, bird, chair, fish, ant, pier, and glasses, each of which contains 20 shapes. In order to fully evaluate the capacity of all methods, we select the most distinctive shape pairs via the following scheme. For a pair of shapes S_i, S_j from the same category, we compute the first 50 eigenvalues Λ_i, Λ_j and the spectral distance $d(S_i, S_j) = \|\Lambda_i - \Lambda_j\|$. We then sample 50 pairs from the overall 190 in the descending order of spectral distances for our test. (2) We further pick ten pairs from the test cases presented in [Yang et al. 2020] for more variability. Finally, we remark that for each pair (S_i, S_j) , we compute maps in both directions.

Evaluation Metrics: To evaluate the maps, we consider four well-known metrics including Dirichlet energy [Ezuz et al. 2019], Coverage (*i.e.* surjectivity) [Huang and Ovsjanikov 2017], Geodesic matching error with respect to ground truth landmark labels [Kim et al. 2011], and Bijection [Ren et al. 2018]. We refer readers to the Supp. Mat. for the details on these metrics.

4.3 3D Shapes Interpolation

In Fig. 6, we visualize interpolations between shapes induced by our learned flow, which are smooth, plausible, and semantically meaningful. Beyond achieving high-quality maps, we believe that they also reveal the potential of our method in generating high-quality 3D assets autonomously.

4.4 Dense Shape Correspondence

We report both quantitative and qualitative results on the involved benchmarks. First of all, we report the average geodesic errors of

Table 2. Average scores regarding over all categories in Tab. 1.

	Dirichlet ↓	Cov. ↑	Lmks. Err. ↓	Bij ↓
MapTree	17.7309	0.3967	0.3683	0.0432
BIM	12.4723	0.4665	0.3200	0.2504
SmoothShells	14.0198	0.6275	0.2221	0.0101
NeuroMorph	22.0461	0.1099	0.1931	0.0944
ENIGMA	6.5344	0.6168	0.3464	0.0123
Ours	6.4702	0.6418	0.0956	0.0075

each test set in Tab. 1. Our method outperforms *all* baselines across *all* sets, with significant margins in the categories of airplane, ant, bird, chair, glasses, plier and EBCM.

In total, **SRIF** achieves an average Geodesic Error of 0.0956, which is less than half of the second-best baseline. Our method even outperforms ENIGMA in Dirichlet Energy – our method does not explicitly optimize for this metric while ENIGMA uses RHM [Ezuz et al. 2019] for post-processing, which minimizes Dirichlet energy. Fig. 10 showcases part of the qualitative results, which agree nicely with the quantitative results. One obvious problem among the intrinsic-based method (BIM, MapTree, Enigma) is symmetry ambiguity. Though our method gets rid of such by extrinsic alignment, we argue that such a requirement is indeed easier to meet than injecting orientation information into intrinsic-based methods. Moreover, in the Supp. Mat., we also report the scores of ENIGMA with allowance on the symmetric flip (as in the regarding paper), yet our method still outperforms it across all sets with more restrictive evaluation.

We further consider cross-category pairs in Fig. 5. Though both methods produce distorted maps in the two challenging pairs, our method better captures the structural correspondences between shapes (see the red boxes).

4.5 Point-based SRIF

In fact, **SRIF** can be directly applied on *unstructured point clouds*. The only two parts in Sec. 3 where we utilize mesh information are multi-view rendering and the construction of local neighborhoods for ARAP regularization. For the former, the Open3D library supports rendering point clouds, despite of a certain degree of detail loss; For the latter, one can approximate Euclidean proximity among vertices. As shown in Fig. 7, our framework manages to deliver high-quality correspondences with less structured input. This is in sharp contrast to methods heavily depending on surface geometry, for instance, the spectral-based shape matching techniques.

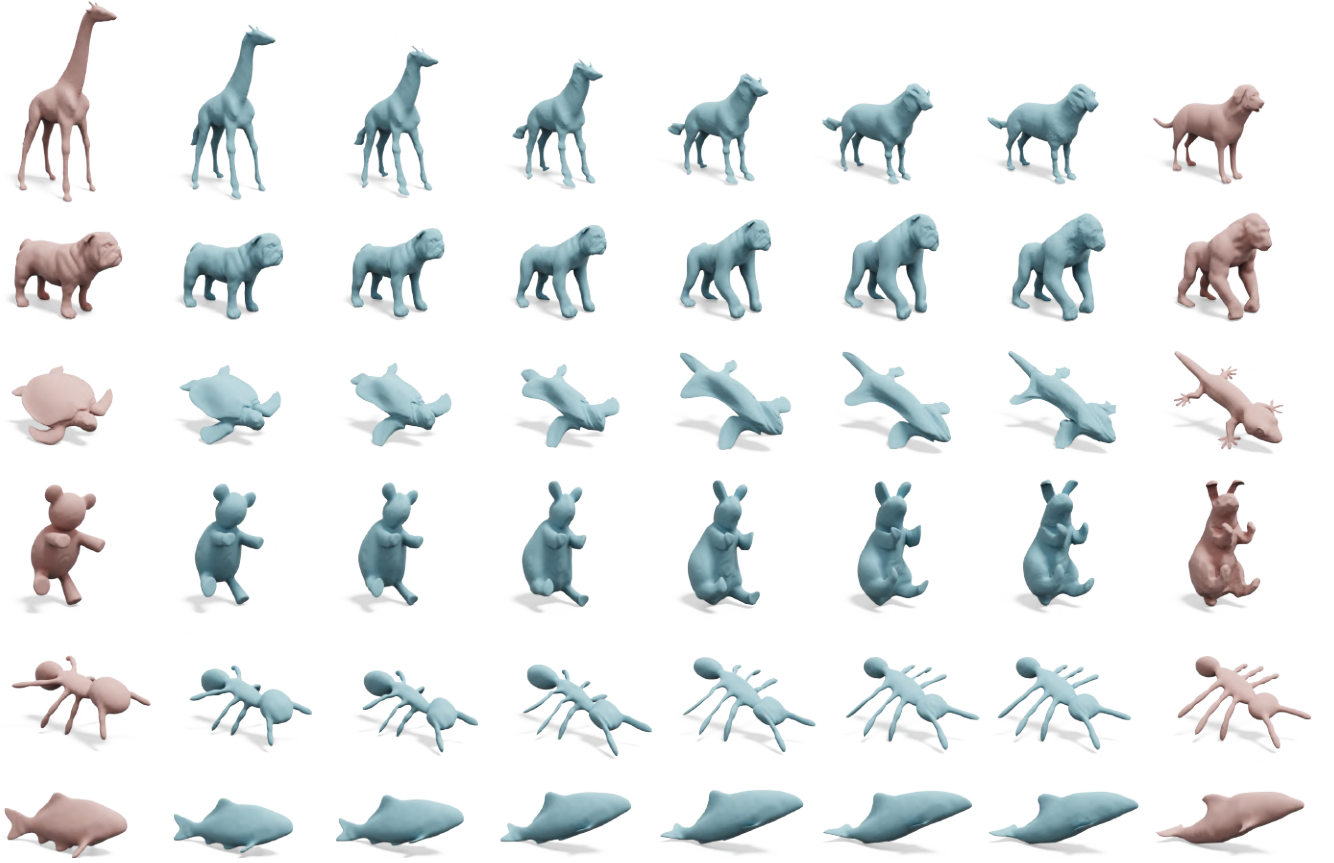


Fig. 6. Demonstrations of smooth and semantically meaningful shape interpolations obtained by our estimated flow.

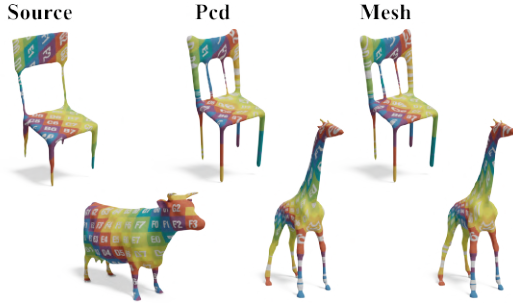


Fig. 7. Our framework can be directly applied to unstructured point clouds. We visualize maps computed with point cloud input (middle) and mesh input (right). Both maps are comparable and semantically meaningful.

4.6 Robustness

We demonstrate the our robustness in the following perspectives:
Mesh Quality: In practice, meshes can exhibit severe irregularities. For instance, the shapes in the right-most and left-most columns of Fig. 8 are from KeyPointNet dataset [You et al. 2020], which consist

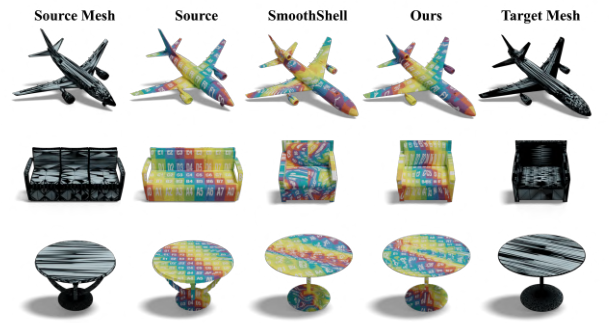


Fig. 8. In practice, meshes can exhibit server irregularities (left-most and right-most columns). Our method demonstrates clearly better robustness than SmoothShells (top and middle rows), while can fail in the presence of large topological changes (bottom row).

of a large portion of thin triangles. This can pose significant challenges on registration methods based on triangulation and point-wise correspondence update. For instance, in the top row of Fig. 8,

Table 3. We validate the robustness of our method to rotation on one pair by rotating the target around the X, Y, Z axes by 10, 30, and 45 degrees, respectively, and calculating the landmark errors.

	0	10	30	45
X		0.0529	0.0535	0.0549
Y	0.0529	0.0555	0.0563	0.0565
Z		0.0549	0.0551	0.0657

Table 4. Comparison to several variants of our method on the pair shown in Fig. 2, see the main text for details.

	Dirichlet ↓	Cov. ↑	Lmks. Err. ↓	Bij ↓
Direct flow est.	16.1538	0.2881	0.1157	0.0463
w/o surface ext.	6.9506	0.6988	0.0665	0.0069
w/ 3D-GS	8.9399	0.5536	0.0833	0.0159
4 views	7.7054	0.6917	0.0764	0.0072
8 views	6.6097	0.6963	0.0663	0.007
Full	6.3094	0.7031	0.0529	0.0064

SmoothShells cannot match the airplanes even though they are similar to each other. In contrast, thanks to the flow estimation module, our method enjoys stronger robustness on this front.

Rotational Perturbation: We generally assume the shapes of interest are extrinsically aligned, which is a common practice in shape registration [Yao et al. 2023]. Meanwhile, we empirically observe that **SRIF** is robust with rotational perturbation as large as 45 degrees (see Tab. 3 and qualitative results in the Supp. Mat.). We attribute such to the fact that the diffusion model is trained with objects in various orientations [El Banani et al. 2024], thus gaining certain robustness and passing to our framework.

4.7 Ablation Studies

Intermediate geometry: It is worth noting that our flow estimation can be conducted with as few as two shapes. We report the direct estimation in the first row of Tab. 4, which clearly suggests the necessity of applying LVM to achieve the intermediate point clouds. At the same time, we ablate the surface point cloud extraction and use the original Gaussian for guidance, whose absence causes performance degradation.

Reconstruction Method: We perform dynamic 3D-GS on the whole set of multi-view interpolated images. One can as well independently perform 3D Gaussian Splatting [Kerbl et al. 2023] on the multi-view images at each time step to obtain the intermediate geometry. The third row of Tab. 4 suggests that the above variant is suboptimal. This is probably since image interpolation is performed *independently* from each viewpoint, therefore it is hard to guarantee the multi-view consistency at each time step.

View Number is an important hyper-parameter of our method, in the fourth and fifth row of Tab. 4, we ablate it by testing with fewer views. It is evident that a larger number of views is advantageous, as it naturally covers more thoroughly the shapes of interest. Of course, as will be discussed in Sec. 4.8, increasing the view number would significantly slow down the method, we choose 16 with a trade-off of efficiency and accuracy.

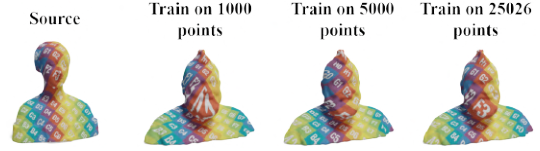


Fig. 9. We test the robustness of our flow estimation to the number of input points. We train it on 1,000 points, 5,000 points, and the original 25,026 points, respectively, and conduct the tests on the original point cloud.

4.8 Running Time Analysis

We compare time efficiency of our method and baselines with respect to a fixed pair of shapes on the same machine (see the Supp. Mat. for details). MapTree, BIM, NeuroMorph all take 1 min, and SmoothShells takes 5 mins. ENIGMA is ran by the authors, who report running time of 20 mins to process shapes of 5000 vertices with post-refinement. Our method takes 40 mins (20 mins for image morphing, 10 mins for intermediate point clouds generation, and 10 mins for flow estimation). The complexity of image morphing and 3D Gaussian reconstruction is determined by the number of views and interpolating images. The complexity of flow estimation depends on the number of vertices on \mathcal{S} .

While efficiency remains the main bottleneck, we highlight that, compared to the baselines, our method achieves significantly more precise maps but also high-quality morphing process across various categories. Furthermore, since our flow estimation module can learn a continuous flow with finite discrete point clouds, we can downsample \mathcal{S} and follow the strategy in Sec. 4.5 to alleviate the computational burden. As shown in Fig. 9, significant down-sampling leads to a reasonable performance drop. We finally emphasize that the flow trained on the down-sampled point cloud can be inferred on the original one directly, without any post-processing.

5 CONCLUSION AND LIMITATIONS

In this paper, we propose **SRIF**, an autonomous framework for semantic 3D shape registration. By exploiting semantic information obtained from LVMs in a dynamic manner and with a novel flow estimation module, **SRIF** achieves high-quality dense correspondences on challenging shape pairs, but also delivers smooth, semantically meaningful interpolation as a by-product. Ablation studies justify our overall design and highlight the robustness and scalability of our framework.

We identify the following limitations of our method, which lead to future work directions: 1) There exists significant room for improvement on efficiency. As shown in Sec. 4.8, the main bottleneck of our pipeline lies in image morphing, or, more specifically, LoRA fine-tuning, which takes over 50% of the total running time. To

Table 5. Mean geodesic errors on the SMPL and SHREC19 dataset.

	Maptree	BIM	SS	NM	Ours
SMPL	0.1715	0.1329	0.0354	0.1017	0.0696
SHREC19	0.3013	0.2174	0.0685	0.1499	0.0823

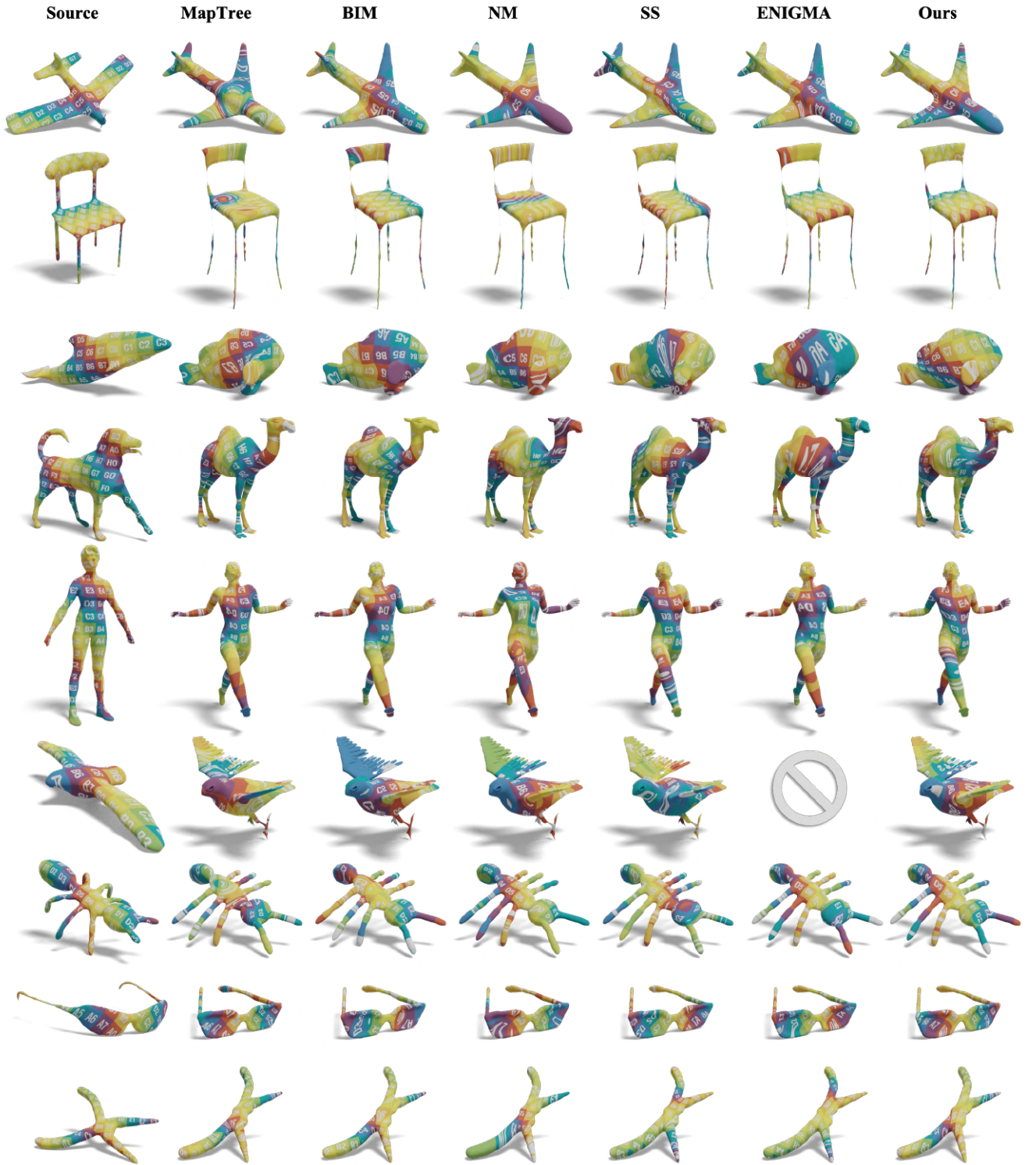


Fig. 10. Qualitative comparisons on various categories from SHREC'07 [Giorgi et al. 2007]. ENIGMA [Edelstein et al. 2020] fails to return result on the pair of birds. Note that the target chair in the second row is *not* disconnected – It appears so due to the thin structure within the chair.

this end, we plan to resort to advances in parameter efficient fine-tuning; 2) Our method does not guarantee the output to be continuous or bijective. It would be interesting to explore how to regularize the smoothness of flow [Dupuis et al. 1998]; on the other hand, since flow is by construction invertible, we can encourage bijectivity by taking forward and backward flow simultaneously during training; 3) Since our method leverages image interpolation, it could be suboptimal when the intermediate results are problematic. To see that, we evaluate our method on SHREC19 [Melzi et al. 2019] and SMPL [Loper et al. 2015] dataset. As shown in Tab. 5, our method is outperformed by SmoothShells, which leverages intrinsic geometry information, with a notable margin. We attribute the failure to two factors: first human articulation spans a large space, which might not be well learnt by diffusion models without explicit modeling; second there exist self-occlusions among the multi-view renderings of human shapes. We refer readers to the Supp. Mat. for more details on this experiment. We plan to introduce stronger prior on this front, say, leveraging pre-trained model on human shapes/images. 4) Our method uses ARAP to regularize mesh deformation, which implicitly encourages local neighborhood preservation. This in turn prevents our method from characterizing significant topological changes (see bottom row of Fig. 8, where the supports of tables are distinctive). As shown in Sec. 4.5, our method can be adapted into purely point-based settings, it is interesting to further exploit this property.

Acknowledgement. This work was supported by the National Natural Science Foundation of China under contract No. 62171256 and Meituan.

A APPENDIX

In this supplementary material, we provide ablation on our color scheme of choice (Sec. A.1); more details about the surface point extraction module (Sec. A.2); detailed formulations on the metrics (Sec. A.3); qualitative results on robustness regarding misalignment (Sec. A.4); qualitative comparison to landmark-based approach (Sec. A.5); details on the non-rigid human shape matching in Sec. 5 of the main paper (Sec. A.6); details on running time analysis (Sec. A.7); per-category quantitative results regarding Tab.1 in the main paper (Sec. A.8).

A.1 Ablation study on color scheme for rendering

As we put no assumption on the texture of 3D shapes of interest, the rendered images often suffer from loss of details. On the other hand, diffusion models are trained on realistic images with rich texture. To compensate the discrepancy, we design a specific color coding scheme to add more texture details.

In this part, we compare the effect of three different color schemes, including textureless rendering, normal-based color scheme, and the one proposed in Sec.3.1 of the main paper. As shown in Fig 11, our color scheme yields the most natural and complete interpolation between an airplane and a bird. The rest two, on the other hand, suffer from either missing frames or missing parts.

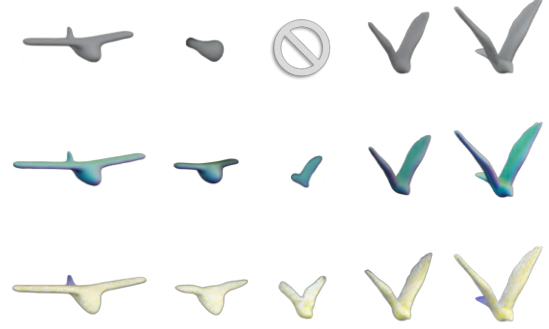


Fig. 11. We use 3 different color schemes to render the mesh. The first row shows rendering without textures, and the object disappears in the middle frame. The second row shows rendering with normal vector coloring, and the right wing of the target bird is still close to disappearing. The third row shows our coloring method, where the interpolation sequence is smooth and plausible.

A.2 Details on surface point extraction module

Figure 12 shows our surface points extraction operation. We assume to be given an input point cloud \mathcal{P} as well as a set of camera positions $\mathcal{E} = \{\mathbf{e}_1, \mathbf{e}_2, \dots, \mathbf{e}_N\}$ distributed on a sphere surrounding the point cloud. For each camera position \mathbf{e}_i , the camera is configured with parameters including the field of view θ , center point \mathbf{c} , and up vector \mathbf{u} . A depth image \mathcal{D}_i is rendered from the perspective of the current camera position. The rendered depth image \mathcal{D}_i is then unprojected to obtain the corresponding 3D points \mathcal{Q}_i in the world coordinate system.

$$\mathbf{q} = \mathcal{U}(\mathbf{p}, \mathcal{D}_i(x, y), w, h), \quad (5)$$

where \mathbf{q} is the unprojected 3D point, $\mathbf{p} = (x, y)$ is a pixel in the depth image, and w and h are the width and height of the depth image, respectively.

Intuitively, the inner points are filtered out through a combination of forward depth image rendering and inverse unprojection. In other words, only points around the surface are extracted.

A.3 Evaluation Metrics

We use the following evaluation metrics to assess the quality of the generated maps and registration results.

Dirichlet Energy: The Dirichlet energy measures the smoothness of the mapping between the source and target shape. It is defined as:

$$E_D(f) = \frac{1}{2} \int_S |\nabla f|^2 dA, \quad (6)$$

where $f : \mathcal{S} \rightarrow \mathcal{T}$ is the mapping between the source shape \mathcal{S} and the target shape \mathcal{T} , and ∇f denotes the gradient of f . A lower Dirichlet energy indicates a smoother mapping.

Coverage (surjectivity): Coverage evaluates the extent to which the target shape is covered by the mapped image of the source

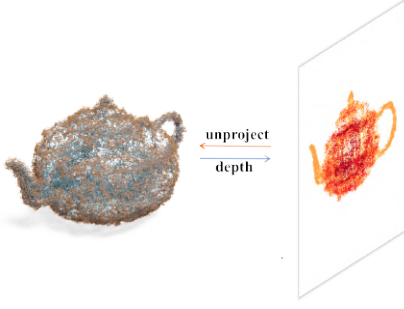


Fig. 12. Our surface point extraction module operates by projecting and unprojecting depth images from multiple viewpoints. To better illustrate our method, we only show one viewpoint in the figure.

shape. It is defined as:

$$\text{Coverage}(f) = \frac{|\{q \in \mathcal{T} : \exists p \in \mathcal{S}, f(p) = q\}|}{|\mathcal{T}|}, \quad (7)$$

where $|\cdot|$ denotes the cardinality of a set. A higher Coverage score suggests a more injective mapping.

Landmark Error: This metric assesses the accuracy of the mapping by comparing it against ground truth landmark correspondences. Given a set of landmark pairs (p_i, q_i) , where $p_i \in \mathcal{S}$ and $q_i \in \mathcal{T}$, the matching error is defined as:

$$\text{Landmark Error}(f) = \frac{1}{n} \sum_{i=1}^n \frac{d(f(p_i), q_i)}{\sqrt{\text{area}(\mathcal{T})}}, \quad (8)$$

where $d(\cdot, \cdot)$ is the geodesic distance, n is the number of landmark pairs and $\sqrt{\text{area}(\cdot)}$ is a normalizing factor. A lower matching error indicates a more accurate mapping.

Bijectivity: Let \mathcal{S} denote the source point cloud and \mathcal{T} denote the target point cloud. We define M_{12} as the mapping from \mathcal{S} to \mathcal{T} and M_{21} as the mapping from \mathcal{T} to \mathcal{S} . Furthermore, let $M_{11} = M_{12}(M_{21})$ and $M_{22} = M_{21}(M_{12})$. The transformation error can be quantified using the following expressions:

$$\mathbf{V}_S = \text{vec}(\text{normv}(\mathcal{S} - \mathcal{S}[M_{11}])) \quad (9)$$

$$\mathbf{V}_T = \text{vec}(\text{normv}(\mathcal{T} - \mathcal{T}[M_{22}])) \quad (10)$$

$$\text{Bijectivity} = \frac{\frac{1}{n} \sum_{i=1}^n \mathbf{V}_S^i + \frac{1}{m} \sum_{j=1}^m \mathbf{V}_T^j}{2}, \quad (11)$$

where $\mathcal{S}[M_{11}]$ represents the points in \mathcal{S} after applying the mapping M_{11} , and $\mathcal{T}[M_{22}]$ represents the points in \mathcal{T} after applying the mapping M_{22} . Here, $\text{vec}(\cdot)$ denotes the vectorization operation, and $\text{normv}(\cdot)$ denotes the computation of the norm of the vectors.

A.4 Robustness regarding misalignment

We provide visualizations corresponding to Tab.3 of the main paper as shown in Fig. 13. Fixing the source shape, we rotate the target shape around the X, Y, and Z axes by 45 degrees, respectively. Thanks to the strong robustness of LVM regarding rotational perturbations in images, we can obtain reasonable image interpolation

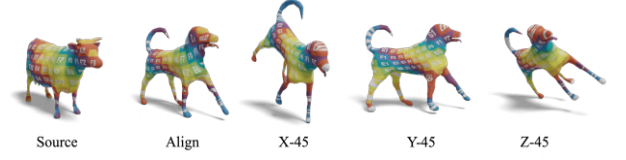


Fig. 13. We initially rotate the target shape by 45 degrees along the X, Y, and Z axes, respectively. The texture visualization indicates that our method is relatively robust to rotation.

results, which can provide appropriate guidance during the registration process. Fig. 13 demonstrates that, without explicitly optimizing for rotation, our method maintains good robustness to rotations of up to 45 degrees.

A.5 Qualitative comparison to SMAT

To further evaluate the plausibility of our results, we apply SMAT on 6 challenging pairs from Fig. 10 of the main paper in Fig. 14 and compare the results with ours. Note that we feed in all available landmarks to SMAT, and that our method achieves comparable results with SMAT while being fully automatic.

A.6 Non-rigid shape matching

In this section, we discuss the performance of our method on datasets with significant pose variations. We selected the following two datasets:

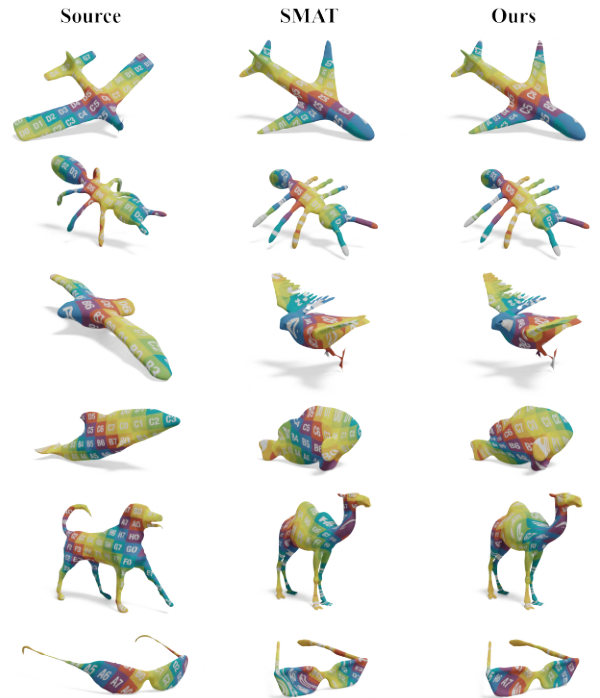


Fig. 14. Qualitative comparisons between **SRIF** and **SMAT**. Note the latter consumes ground-truth landmarks as input, while **SRIF** is fully automatic.



Fig. 15. We evaluate our method on a pair of human shapes undergoing large non-rigid deformations. Top row: Image interpolation; Bottom row: Intermediate point cloud reconstructions.



Fig. 16. We test the running time of all the methods on this pair.

For SHREC19 [Melzi et al. 2019], we evaluate 407 pairs of data with ground truth. In particular, we exclude 23 pairs related to a partial shape. For SMPL [Loper et al. 2015], we randomly generate a set of 500 shapes using SMPL model. And then sample 20 shapes from them via FPS in the pose parameters of generation. Subsequently, similar to the procedure in Sec.4.2 of the main text, we construct 50 pairs among the 20 shapes for inference. As shown in Tab. 5 of the main text, our method is outperformed by SmoothShells with a noticeable margin.

To investigate the failure cause, we examine the intermediate results of our pipeline. As shown in Fig. 15, when there are significant differences in the pose, the image interpolation module [Zhang et al. 2023] struggles to return plausible results (top row), which is further amplified in the follow-up point cloud reconstruction (bottom row). Such discrepancy then leads to the suboptimal solution of our method on this benchmark.

A.7 Running Time analysis

We test MapTree, SmoothShells, NeuroMorph, BIM and our method on the same device, which includes an NVIDIA V100 GPU, a single-core 2.8GHz CPU, and 500MB of memory. The test pair is shown in Fig 16, where the source mesh contains 5400 points and the target mesh contains 5619 points.

In particular, we evaluate MapTree¹, SmoothShells², NeuroMorph³, and BIM on all the test data with the regarding official implementations. Regarding ENIGMA, since the code is not publicly available, we asked the authors to run baseline evaluation, who also reported that ENIGMA took 20 mins to match shapes of 5000 vertices with RHM [Ezuz et al. 2019] as post-refinement.

A.8 Per-category result analysis

We report the scores regarding the four metrics in Sec. A.3 for each category in Tab. 6 as a supplement to Tab.1 in the main paper.

Considering symmetry in the results for ENIGMA, our outcomes are superior in four out of five categories compared to ENIGMA.

We also provide accumulated error curves of the ten categories in Fig. 17. It is evident that in the categories of airplane, chair, ant, bird, glasses, plier, and EBCM, our method’s landmark error reduction is prominent. Indeed, our method gains at least 40% improvement upon the second-best results.

We also provide more shape morphing results in Fig. 18.

REFERENCES

- Ahmed Abdelreheem, Abdelrahman Eldesokey, Maks Ovsjanikov, and Peter Wonka. 2023a. Zero-Shot 3D Shape Correspondence. In *Siggraph Asia*.
- Ahmed Abdelreheem, Ivan Skorokhodov, Maks Ovsjanikov, and Peter Wonka. 2023b. SATR: Zero-Shot Semantic Segmentation of 3D Shapes. In *ICCV*.
- Noam Aigerman, Roi Poranne, and Yaron Lipman. 2015. Seamless Surface Mappings. In *ACM TOG*.
- Brian Amberg, Sami Romdhani, and Thomas Vetter. 2007. Optimal Step Nonrigid ICP Algorithms for Surface Registration. (2007).
- Dragomir Anguelov, Praveen Srinivasan, Daphne Koller, Sebastian Thrun, Jim Rodgers, and James Davis. 2005. SCAPE: Shape Completion and Animation of People. (2005).
- Andreas Blattmann, Robin Rombach, Huan Ling, Tim Dockhorn, Seung Wook Kim, Sanja Fidler, and Karsten Kreis. 2023. Align your latents: High-resolution video synthesis with latent diffusion models. In *Proceedings of the IEEE/CVF Conference on Computer Vision and Pattern Recognition*. 22563–22575.
- Alexander M. Bronstein, Michael M. Bronstein, and Ron Kimmel. 2006. Generalized multidimensional scaling: A framework for isometry-invariant partial surface matching. *PNAS* (2006).
- Yu Deng, Jiaolong Yang, and Xin Tong. 2021. Deformed Implicit Field: Modeling 3D shapes with Learned Dense Correspondence. In *CVPR*.
- Paul Dupuis, Ulf Grenander, and Miller Michael. 1998. Variational problems on flows of diffeomorphisms for image matching. *Quart. Appl. Math.* (1998).
- Michal Edelstein, Danielle Ezuz, and Mirela Ben-Chen. 2020. ENIGMA: Evolutionary Non-Isometric Geometry Matching. (2020).
- Marvin Eisenberger, Zorah Lahner, and Daniel Cremers. 2020. Smooth Shells: Multi-Scale Shape Registration With Functional Maps. In *CVPR*.
- Marvin Eisenberger, David Novotny, Gael Kerchenbaum, Patrick Labatut, Natalia Neverova, Daniel Cremers, and Andrea Vedaldi. 2021. Neuromorph: Unsupervised shape interpolation and correspondence in one go. In *CVPR*.
- Mohamed El Banani, Amit Raj, Kevis-Kokitsi Maninis, Abhishek Kar, Yuanzhen Li, Michael Rubinstein, Deqing Sun, Leonidas Guibas, Justin Johnson, and Varun Jampani. 2024. Probing the 3D Awareness of Visual Foundation Models. In *CVPR*.
- Danielle Ezuz, Justin Solomon, and Mirela Ben-Chen. 2019. Reversible Harmonic Maps Between Discrete Surfaces. *ACM Trans. Graph.* 38, 2, Article 15 (March 2019), 12 pages.
- Daniela Giorgi, Silvia Biasotti, and Laura Paraboschi. 2007. Shape retrieval contest 2007: Watertight models track. *SHREC competition* (2007).
- Antoine Guédon and Vincent Lepetit. 2023. SuGaR: Surface-Aligned Gaussian Splatting for Efficient 3D Mesh Reconstruction and High-Quality Mesh Rendering. *arXiv preprint arXiv:2311.12775* (2023).
- Chen Guo, Xu Chen, Jie Song, and Otmar Hilliges. 2021. Human performance capture from monocular video in the wild. In *3DV*.
- Jonathan Ho, Ajay Jain, and Pieter Abbeel. 2020. Denoising diffusion probabilistic models. In *NeurIPS*.

¹https://github.com/llorz/SGA20_mapExplor

²<https://github.com/marvin-eisenberger/smooth-shells>

³<https://github.com/facebookresearch/neuromorph>

Table 6. Quantitative results of the test cases shown in Fig.8 of the main submission. SS stands for SmoothShell, and NM stands for NeuroMorph. For Enigma, we follow their symmetric setup by calculating the error of both forward and reverse mapping in the SHREC07 categories and taking the minimum of these two as the final result. The former and latter landmarks errors correspond to the outcomes of the forward mapping and the symmetric result, respectively.

		Dirichlet ↓	Cov. ↑	Lmks. Err. ↓	Bij ↓			Dirichlet ↓	Cov. ↑	Lmks. Err. ↓	Bij ↓
airplane	ENIGMA	2.5703	0.6716	0.35\0.25	0.0059	ant	ENIGMA	8.3737	0.6429	0.37\0.25	0.0069
	Maptree	14.1676	0.3633	0.5634	0.0487		Maptree	13.2092	0.2680	0.2635	0.0589
	BIM	3.4598	0.6525	0.2589	0.2223		BIM	8.5061	0.6230	0.3050	0.2347
	SS	7.3184	0.7362	0.2749	0.0064		SS	12.0404	0.7430	0.2694	0.0073
	NM	8.1679	0.1127	0.1510	0.0831		NM	16.0912	0.0842	0.1895	0.0940
	Ours	2.3427	0.7557	0.0356	0.0039		Ours	7.5907	0.6868	0.1133	0.0068
chair	ENIGMA	4.1129	0.5529	0.45\0.31	0.0075	bird	ENIGMA	8.2018	0.3350	0.33\0.28	0.0153
	Maptree	19.9621	0.3208	0.4742	0.0554		Maptree	9.7311	0.2110	0.4117	0.0564
	BIM	32.2091	0.3579	0.4800	0.3160		BIM	8.3057	0.3333	0.4123	0.2888
	SS	28.3655	0.5755	0.2627	0.0321		SS	26.5909	0.3694	0.3009	0.0193
	NM	18.0280	0.0266	0.1853	0.0922		NM	13.5221	0.0895	0.1672	0.1178
	Ours	5.6372	0.6127	0.0295	0.0052		Ours	5.8626	0.5880	0.0965	0.0121
fish	ENIGMA	2.3935	0.7360	0.17\0.14	0.0055	glasses	ENIGMA	5.6478	0.7372	0.68\0.32	0.0175
	Maptree	10.2440	0.6344	0.2949	0.0271		Maptree	9.0106	0.5915	0.6878	0.0376
	BIM	4.2617	0.6656	0.2699	0.1567		BIM	31.3520	0.5013	0.6134	0.4158
	SS	4.7195	0.7927	0.1032	0.0048		SS	9.7207	0.7547	0.3100	0.0177
	NM	13.9717	0.1584	0.1366	0.0787		NM	9.2590	0.0753	0.2652	0.1437
	Ours	3.1247	0.7668	0.0804	0.0040		Ours	5.6394	0.7580	0.0614	0.0102
fourleg	ENIGMA	4.5125	0.3133	0.25\0.19	0.0130	plier	ENIGMA	16.5595	0.7656	0.44\0.31	0.0145
	Maptree	11.0492	0.2260	0.3507	0.0426		Maptree	34.3151	0.4657	0.2805	0.0371
	BIM	8.8194	0.2846	0.2449	0.2010		BIM	15.3346	0.7045	0.5197	0.3149
	SS	8.8495	0.3233	0.1234	0.0116		SS	19.0768	0.8010	0.3900	0.0081
	NM	18.4938	0.0692	0.1697	0.1070		NM	36.0034	0.1251	0.2830	0.1055
	Ours	6.2250	0.3512	0.0824	0.0114		Ours	13.2623	0.7508	0.1476	0.0080
human	ENIGMA	4.8419	0.8108	0.29\0.14	0.0075	ebcm	ENIGMA	5.8304	0.6026	0.3032	0.0060
	Maptree	14.6992	0.3532	0.2633	0.0373		Maptree	26.667	0.5331	0.4231	0.031
	BIM	7.1003	0.5037	0.1810	0.1205		BIM	5.3741	0.5456	0.2968	0.2305
	SS	8.7462	0.5304	0.1572	0.0164		SS	14.7793	0.6495	0.4476	0.0059
	NM	28.5119	0.0798	0.2141	0.0997		NM	59.3832	0.2509	0.1844	0.0437
	Ours	8.6968	0.5394	0.1467	0.0100		Ours	6.3403	0.6784	0.0886	0.0038

Ruqi Huang and Maks Ovsjanikov. 2017. Adjoint Map Representation for Shape Analysis and Matching. In *Computer Graphics Forum*, Vol. 36. Wiley Online Library, 151–163.

Yi-Hua Huang, Yang-Tian Sun, Ziyi Yang, Xiaoyang Lyu, Yan-Pei Cao, and Xiaojuan Qi. 2024. SG-GS: Sparse-Controlled Gaussian Splatting for Editable Dynamic Scenes. In *CVPR*.

Nikhil Keetha, Jay Karhade, Krishna Murthy Jatavallabhula, Gengshan Yang, Sebastian Scherer, Deva Ramanan, and Jonathon Luiten. 2023. Splatam: Splat, track & map 3d gaussians for dense rgb-d slam. *arXiv preprint arXiv:2312.02126* (2023).

Bernhard Kerbl, Georgios Kopanas, Thomas Leimkühler, and George Drettakis. 2023. 3D Gaussian Splatting for Real-Time Radiance Field Rendering. *ACM Transactions on Graphics* 42, 4 (July 2023).

Vladimir G Kim, Yaron Lipman, and Thomas Funkhouser. 2011. Blended Intrinsic Maps. In *ACM Transactions on Graphics (TOG)*, Vol. 30. ACM, 79.

Matthew Loper, Naureen Mahmood, Javier Romero, Gerard Pons-Moll, and Michael J. Black. 2015. SMPL: A Skinned Multi-person Linear Model. *TOG* 34, 6 (2015), 248:1–248:16.

Manish Mandad, David Cohen-Steiner, Leif Kobbelt, Pierre Alliez, and Mathieu Desbrun. 2017. Variance-Minimizing Transport Plans for Inter-surface Mapping. In *ACM TOG*.

S. Melzi, R. Marin, E. Rodolà, U. Castellani, J. Ren, A. Poulénard, P. Wonka, and M. Ovsjanikov. 2019. Matching Humans with Different Connectivity. In *Eurographics Workshop on 3D Object Retrieval*.

Luca Morreale, Noam Aigerman, Vladimir G. Kim, and Niloy J. Mitra. 2024. Semantic Neural Surface Maps. In *Eurographics*.

OpenAI. 2023. *GPT-4 Technical Report*. Technical Report. OpenAI.

Maxime Oquab, Timothée Darcet, Theo Moutakanni, Huy V. Vo, Marc Szafraniec, Vasil Khalidov, Pierre Fernandez, Daniel Haziza, Francisco Massa, Alaaeldin El-Nouby, Russell Howes, Po-Yao Huang, Hu Xu, Vasu Sharma, Shang-Wen Li, Wojciech Galuba, Mike Rabbat, Mido Assran, Nicolas Ballas, Gabriel Synnaeve, Ishan Misra, Herve Jegou, Julien Mairal, Patrick Labatut, Armand Joulin, and Piotr Bojanowski. 2023. DINOv2: Learning Robust Visual Features without Supervision.

Maks Ovsjanikov, Mirela Ben-Chen, Justin Solomon, Adrian Butscher, and Leonidas Guibas. 2012. Functional Maps: A Flexible Representation of Maps Between Shapes. *ACM Transactions on Graphics (TOG)* 31, 4 (2012), 30.

Besl PJ and McKay ND. 1992. A method for registration of 3-d shapes. (1992), 239–256.

Alec Radford, Jong Wook Kim, Chris Hallacy, Aditya Ramesh, Gabriel Goh, Sandhini Agarwal, Girish Sastry, Amanda Askell, Pamela Mishkin, Jack Clark, Gretchen Krueger, and Ilya Sutskever. 2021. Learning Transferable Visual Models From Natural Language Supervision. In *ICML*.

Jing Ren, Simone Melzi, Maks Ovsjanikov, and Peter Wonka. 2020. MapTree: Recovering Multiple Solutions in the Space of Maps. *ACM TOG* (2020).

Jing Ren, Adrien Poulénard, Peter Wonka, and Maks Ovsjanikov. 2018. Continuous and Orientation-preserving Correspondences via Functional Maps. *ACM Trans. Graph.* 37, 6, Article 248 (Dec. 2018), 16 pages.

Robin Rombach, Andreas Blattmann, Dominik Lorenz, Patrick Esser, and Björn Ommer. 2022. High-Resolution Image Synthesis with Latent Diffusion Models. In *CVPR*.

P. Schmidt, D. Pieper, and L. Kobbelt. 2023. Surface Maps via Adaptive Triangulations. In *EuroGraphics*.

Christoph Schuhmann, Romain Beaumont, Richard Vencu, Cade Gordon, Ross Wightman, Mehdi Cherti, Theo Coombes, Aarush Katta, Clayton Mullis, Mitchell Wortsman, Patrick Schramowski, Srivatsa Kundurthy, Katherine Crowson, Ludwig

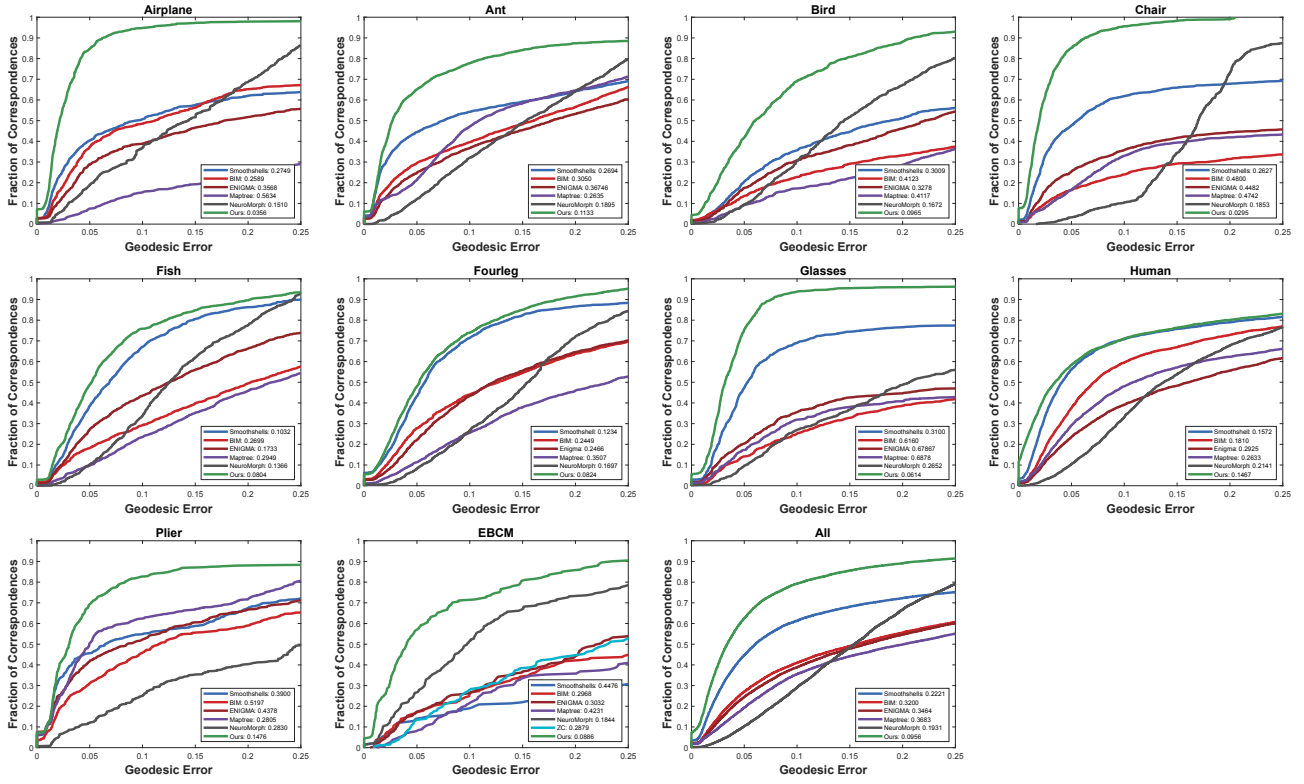


Fig. 17. Accuracy evaluation of our method and baselines on 10 test sets. The curves read the fraction (Y-axis) of computed correspondences that fall within certain normalized geodesic distance to the ground-truth ones (X-axis). The numbers in the legends show the average error. Our method achieves the best accuracy over *all* sets.

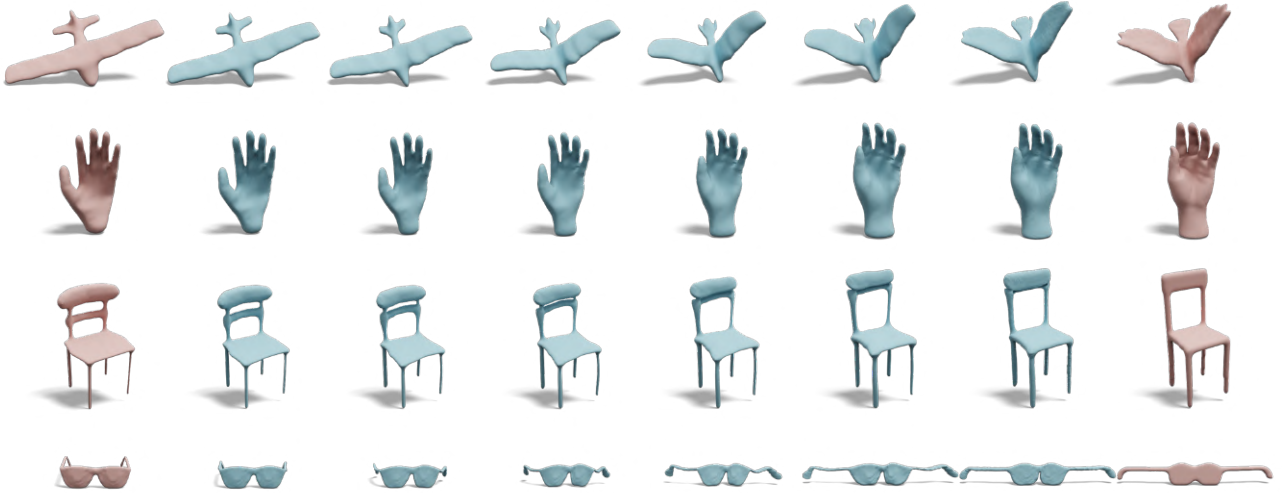


Fig. 18. Demonstrations of smooth and semantically meaningful shape interpolations obtained by our estimated flow.

- Schmidt, Robert Kaczmarczyk, and Jenia Jitsev. 2022. LAION-5B: An open large-scale dataset for training next generation image-text models.
- Robert W Sumner and Jovan Popović. 2004. Deformation transfer for triangle meshes. In *ACM Transactions on Graphics (TOG)*, Vol. 23. ACM, 399–405.
- Bo Sun, Xiangru Huang, Zaiwei Zhang, Junfeng Jiang, Qixing Huang, and Chandrajit Bajaj. 2021. ARAPReg: An As-Rigid-As Possible Regularization Loss for Learning Deformable Shape Generators. In *ICCV*.
- Gary KL Tam, Zhi-Quan Cheng, Yu-Kun Lai, Frank C Langbein, Yonghui Liu, David Marshall, Ralph R Martin, Xian-Fang Sun, and Paul L Rosin. 2013. Registration of 3D point clouds and meshes: a survey from rigid to nonrigid. *IEEE transactions on visualization and computer graphics* 19, 7 (2013), 1199–1217.
- Clinton J Wang and Polina Golland. 2023. Interpolating between images with diffusion models. *arXiv preprint arXiv:2307.12560* (2023).
- Thomas Wimmer, Peter Wonka, and Maks Ovsjanikov. 2024. Back to 3D: Few-Shot 3D Keypoint Detection with Back-Projected 2D Features. In *Proceedings of the IEEE/CVF Conference on Computer Vision and Pattern Recognition*.
- Guandao Yang, Xun Huang, Zekun Hao, Ming-Yu Liu, Serge Belongie, and Bharath Hariharan. 2019. Pointflow: 3d point cloud generation with continuous normalizing flows. In *Proceedings of the IEEE/CVF international conference on computer vision*. 4541–4550.
- Yang Yang, Wenxiang Zhang, Yuan Liu, Ligang Liu, and Xiaoming Fu. 2020. Error-bounded Compatible Remeshing. In *ACM TOG*.
- Ziyi Yang, Xinyu Gao, Wen Zhou, Shaohui Jiao, Yuqing Zhang, and Xiaogang Jin. 2023. Deformable 3D Gaussians for High-Fidelity Monocular Dynamic Scene Reconstruction. *arXiv:2309.13101 [cs.CV]*
- Yuxin Yao, Bailin Deng, Weiwei Xu, and Juyong Zhang. 2023. Fast and robust non-rigid registration using accelerated majorization-minimization. *IEEE Transactions on Pattern Analysis and Machine Intelligence* (2023).
- Yang You, Yujing Lou, Chengkun Li, Zhoujun Cheng, Liangwei Li, Lizhuang Ma, Cewu Lu, and Weiming Wang. 2020. KeypointNet: A Large-scale 3D Keypoint Dataset Aggregated from Numerous Human Annotations. *arXiv preprint arXiv:2002.12687* (2020).
- Tao Yu, Zerong Zheng, Kaiwen Guo, Jianhui Zhao, Qionghai Dai, Hao Li, Gerard Pons-Moll, and Yebin Liu. 2018. Doublefusion: Real-time capture of human performances with inner body shapes from a single depth sensor. In *CVPR*.
- Kaiwen Zhang, Yifan Zhou, Xudong Xu, Xingang Pan, and Bo Dai. 2023. Diff-Morpher: Unleashing the Capability of Diffusion Models for Image Morphing. *arXiv:2312.07409*
- Shihao Zhao, Dongdong Chen, Yen-Chun Chen, Jianmin Bao, Shaozhe Hao, Lu Yuan, and Kwan-Yee K Wong. 2023. Uni-ControlNet: All-in-One Control to Text-to-Image Diffusion Models. *arXiv preprint arXiv:2305.16322* (2023).
- Zerong Zheng, Tao Yu, Qionghai Dai, and Yebin Liu. 2021. Deep Implicit Templates for 3D Shape Representation. In *CVPR*.
- Qian-Yi Zhou, Jaesik Park, and Vladlen Koltun. 2018. Open3D: A Modern Library for 3D Data Processing. (2018). *arXiv:1801.09847*